

The clustering of the SDSS-IV extended Baryon Oscillation Spectroscopic Survey DR16 luminous red galaxy and emission line galaxy samples: cosmic distance and structure growth measurements using multiple tracers in configuration space

Yuting Wang^{1*}, Gong-Bo Zhao^{1,2†}, Cheng Zhao³, Oliver H. E. Philcox^{4,5}, Shadab Alam⁶, Amélie Tamone³, Arnaud de Mattia⁷, Ashley J. Ross⁸, Anand Raichoor³, Etienne Burtin⁷, Romain Paviot^{9,10}, Sylvain de la Torre⁹, Will J. Percival^{11,12,13}, Kyle S. Dawson¹⁴, Héctor Gil-Marín^{15,16}, Julian E. Bautista¹⁷, Jiamin Hou¹⁸, Kazuya Koyama¹⁷, John A. Peacock⁶, Vanina Ruhlmann-Kleider⁷, Héliou du Mas des Bourboux¹⁴, Chia-Hsun Chuang¹⁹, Johan Comparat¹⁸, Stephanie Escoffier¹⁰, Jean-Paul Kneib³, Eva-Maria Mueller²⁰, Jeffrey A. Newman²¹, Graziano Rossi²², Arman Shafieloo²³, Donald P. Schneider²⁴

¹ National Astronomy Observatories, Chinese Academy of Science, Beijing, 100101, P.R.China

² University of Chinese Academy of Sciences, Beijing 100049, P.R.China

³ Institute of Physics, Laboratory of Astrophysics, École Polytechnique Fédérale de Lausanne (EPFL), Observatoire de Sauverny, CH-1290 Versoix, Switzerland

⁴ Department of Astrophysical Sciences, Princeton University, Princeton, NJ 08544, USA

⁵ Harvard-Smithsonian Center for Astrophysics, 60 Garden St., MA, 02138, USA

⁶ Institute for Astronomy, University of Edinburgh, Royal Observatory, Edinburgh, EH9 3HJ, United Kingdom

⁷ IRFU, CEA, Université Paris-Saclay, F-91191 Gif-sur-Yvette, France

⁸ Center for Cosmology and Astro-Particle Physics, Ohio State University, Columbus, Ohio, USA

⁹ Aix Marseille Univ, CNRS, CNES, LAM, Marseille, France

¹⁰ Aix Marseille Univ, CNRS/IN2P3, CPPM, Marseille, France

¹¹ Waterloo Centre for Astrophysics, University of Waterloo, Waterloo, ON N2L 3G1, Canada

¹² Department of Physics and Astronomy, University of Waterloo, Waterloo, ON N2L 3G1, Canada

¹³ Perimeter Institute for Theoretical Physics, 31 Caroline St. North, Waterloo, ON N2L 2Y5, Canada

¹⁴ Department Physics and Astronomy, University of Utah, 115 S 1400 E, Salt Lake City, UT 84112, USA

¹⁵ Institut de Ciències del Cosmos, Universitat de Barcelona, ICCUB, Martí i Franquès 1, E08028 Barcelona, Spain

¹⁶ Institut d'Estudis Espacials de Catalunya (IEEC), E08034 Barcelona, Spain

¹⁷ Institute of Cosmology & Gravitation, University of Portsmouth, Dennis Sciama Building, Portsmouth, PO1 3FX, United Kingdom

¹⁸ Max-Planck-Institut für Extraterrestrische Physik, Postfach 1312, Giessenbachstrasse 1, 85748 Garching bei München, Germany

¹⁹ Kavli Institute for Particle Astrophysics and Cosmology, Stanford University, 452 Lomita Mall, Stanford, CA 94305, USA

²⁰ Sub-department of Astrophysics, Department of Physics, University of Oxford, Denys Wilkinson Building, Keble Road, Oxford OX1 3RH

²¹ PITT PACC, Department of Physics and Astronomy, University of Pittsburgh, Pittsburgh, PA 15260, USA

²² Department of Physics and Astronomy, Sejong University, Seoul 143-747, Korea

²³ Korea Astronomy and Space Science Institute, 776 Daedeokdae-ro, Yuseong-gu, Daejeon 305-348, Republic of Korea

²⁴ Institute for Gravitation and the Cosmos, Pennsylvania State University, University Park, PA 16802, USA

ABSTRACT

We perform a multi-tracer analysis using the complete Sloan Digital Sky Survey IV (SDSS-IV) extended Baryon Oscillation Spectroscopic Survey (eBOSS) DR16 luminous red galaxy (LRG) and the DR16 emission line galaxy (ELG) samples in the configuration space, and successfully detect a cross correlation between the two samples, and find the growth rate to be $f\sigma_8 = 0.342 \pm 0.085$ (~ 25 per cent accuracy) from the cross sample alone. We perform a joint measurement of the baryonic acoustic oscillation (BAO) and redshift space distortion (RSD) parameters at a single effective redshift of $z_{\text{eff}} = 0.77$, using the auto- and cross-correlation functions of the LRG and ELG samples, and find that the comoving angular diameter distance $D_M(z_{\text{eff}})/r_d = 18.93 \pm 0.37$, the Hubble distance $D_H(z_{\text{eff}})/r_d = 19.65 \pm 0.54$, and $f\sigma_8(z_{\text{eff}}) = 0.445 \pm 0.038$, which is consistent with a Λ CDM model at 68% CL. Compared to the single-tracer analysis on the LRG sample, the Figure of Merit (FoM) of α_{\perp} , α_{\parallel} and $f\sigma_8$ is improved by a factor of 1.18 in our multi-tracer analysis, and in particular, the statistical uncertainty of $f\sigma_8$ is reduced by 11.6%.

Key words: large scale structure of the Universe; multi-tracer analysis; cosmological parameters

1 INTRODUCTION

Observations of the large-scale structure of the Universe provide an essential probe of the physics of the accelerating cosmic expansion, which was discovered by the observation of type Ia supernovae (Riess et al. 1998; Perlmutter et al. 1999). The clustering analysis of large-scale structure allows us to measure the cosmic expansion history and structure growth via signals of baryon acoustic oscillations (BAO) and redshift space distortions (RSD), respectively (Cole et al. 1995; Peacock et al. 2001; Cole et al. 2005; Hawkins et al. 2003; Eisenstein et al. 2005; Okumura et al. 2008; Percival & White 2009). The BAO, produced by the competition between gravity and radiation due to the coupling between baryons and photons before the cosmic recombination, leaves an imprint on the distribution of galaxies at late times. After the decoupling of photons, the acoustic oscillations are frozen at a characteristic scale around $\sim 100 h^{-1}\text{Mpc}$, which is determined by the comoving sound horizon at the drag epoch r_d . This feature corresponds to an excess in the 2-point correlation function, or a series of wiggles in the power spectrum (Percival et al. 2001; Cole et al. 2005; Eisenstein et al. 2005), making BAO a robust observable as a cosmic standard ruler. Measuring the BAO scale in the radial and transverse directions provides strong constraints on Hubble expansion rate and angular diameter distance, respectively. The RSD is produced due to peculiar motions of galaxies: galaxies tend to infall towards the local over-density regions, thus the clustering along the line-of-sight (LOS) is enhanced on large scales (Kaiser 1987; Peacock et al. 2001). Thus measuring RSD effect sets a constraint on the growth rate of cosmic structure.

The most precise BAO and RSD measurements to date were reported by the Baryon Oscillation Spectroscopic Survey (BOSS) collaboration using the final Data Release 12 (DR12) (Alam et al. 2015), which contains more than one million galaxies with spectroscopic redshifts. BOSS achieved a (1.0 – 2.5) per cent BAO measurement precision and a 9.2 per cent RSD precision in the redshift range of $0.2 < z < 0.75$ (Alam et al. 2016), and extracted tomographic information of galaxy clustering in the past lightcone (Wang et al. 2017b; Zhao et al. 2017b; Wang et al. 2018b;

Zheng et al. 2019), which is key for probing dynamical dark energy (Zhao et al. 2017a; Wang et al. 2018a). The BOSS DR12 data can provide high-precision constraints on cosmological parameters (Ivanov et al. 2020; D’Amico et al. 2020; Colas et al. 2020; Philcox et al. 2020). The extended BOSS (eBOSS) project, the successor of BOSS, aims to map the Universe using multiple galaxies at higher redshifts, covering the redshift range of $0.6 < z < 2.2$ (Dawson et al. 2016). It allows for BAO and RSD measurements at high redshifts, which is crucial to break degeneracy between key cosmological parameters, *e.g.* H_0 and Ω_m (Wang et al. 2017a).

However, the precision of the measurements of galaxy clustering is restricted by the cosmic variance on large scales due to the limited volume that a galaxy survey can map, and by the shot noise on small scales due to the discreteness of galaxies. One potential way to tackle the cosmic variance is to contrast multiple tracers of the dark matter field with different biases, *i.e.* the ‘multi-tracer’ technique (McDonald & Seljak 2009; Seljak 2009). In the ideal case with no shot noise, the ratio of over-densities of two tracers would be independent of the density field of dark matter, then the measurements of parameters related to the bias parameter can be immune to the cosmic variance, and thus they can be accurately determined. For practical applications, the gain from multiple tracers can be downgraded by various factors including the overlapping redshift ranges and sky regions, the ratio of biases, the Poisson noise of the 2-point function of each tracer, *etc.* Multi-tracer studies of galaxy surveys have been performed; for instance, Blake et al. (2013) found a 10 – 20 per cent improvement on the RSD measurement via the multi-tracer analysis of the Galaxy and Mass Assembly survey (GAMA). This technique was also applied to analysing the galaxy clustering in the overlapping region between the BOSS and WiggleZ surveys (Ross et al. 2014; Beutler et al. 2016; Marín et al. 2016).

The eBOSS survey, which is a part of the Sloan Digital Sky Survey-IV (SDSS-IV) project (Blanton et al. 2017), used the 2.5-metre Sloan telescope (Gunn et al. 2006) located at the Apache Point Observatory in New Mexico. The spectra of samples are collected by the two multi-object fiber spectrographs (Smee et al. 2013). eBOSS is the first survey that can simultaneously observe multiple galaxies with large overlapping areas in a broad redshift range, which is ideal for a multi-tracer analysis. In this paper we present a multi-tracer analysis using the final eBOSS DR16 Lumi-

* Email: ytwang@nao.cas.cn

† Email: gbzhao@nao.cas.cn

nous Red Galaxy (LRG) sample combined with the high redshift tail from BOSS DR12 CMASS (for “Constant stellar Mass”) sample, dubbed ‘LRGpCMASS’ sample, and the eBOSS DR16 Emission Line Galaxy (ELG) sample.

This work is one of a series of papers presenting results based on the final eBOSS DR16 samples. The multi-tracer analysis of the same samples is also performed in Fourier space to complement this work (Zhao et al. 2020b). For the LRG sample, produced by Ross et al. (2020), the correlation function is used to measure BAO and RSD in Bautista et al. (2020), and the analyses of BAO and RSD from power spectrum are discussed in Gil-Marín et al. (2020). The LRG mock challenge for assessing the modelling systematics is described in Rossi et al. (2020). The ELG catalogues are presented in Raichoor et al. (2020), and analyzed in Fourier space (de Mattia et al. 2020) and in configuration space (Tamone et al. 2020), respectively. The clustering catalogue of quasars is generated by Ross et al. (2020). The quasar mock challenge for assessing modelling systematics is described in Smith et al. (2020). The quasar clustering analysis in Fourier space is discussed in Neveux et al. (2020), and in configuration space in Hou et al. (2020). Finally, the cosmological implications from the clustering analyses is presented in Alam et al. (2020).

We introduce the galaxy samples and mock catalogues used in this paper in Sections 2 and 3, respectively. In Section 4, we describe the template of the full shape correlation function, and in Section 5, we show measurements of the correlation function. The methodology of parameter estimation and the fitting result are presented in Sections 6 and 7, respectively. We discuss cosmological implications using in Section 8. Section 9 is devoted to the conclusion. In this paper, we use a fiducial Λ CDM cosmology with parameters: $\Omega_m = 0.307$, $\Omega_b h^2 = 0.022$, $h = 0.6777$, $n_s = 0.96$, $\sigma_8 = 0.8288$. The comoving sound horizon in this cosmology is $r_d^{\text{fid}} = 147.74 \text{ Mpc}$.

2 GALAXY SAMPLES

In this section, we briefly describe the eBOSS DR16 galaxy sample used in the work.

2.1 The eBOSS LRG and BOSS CMASS samples

The target sample of luminous red galaxies was selected from the optical SDSS photometry DR13 (Albareti et al. 2017) and the infrared photometry from the WISE satellite (Lang et al. 2016). The final algorithms for target selection and catalogue generation are described in Prakash et al. (2016) and in a companion paper (Ross et al. 2020). We use the LRG data of the complete 5 years of eBOSS in the redshift range of $0.6 < z < 1.0$. Its volume density distribution as a function of redshift is shown in red curves in Figure 1. The sky coverage of eBOSS DR16 LRG is 2475.51 deg^2 in the North Galactic Cap (NGC) and 1626.80 deg^2 in the South Galactic Cap (SGC), which are shown in red regions of Figure 2.

In order to correct for observational effects, the eBOSS DR16 LRG catalogue is assigned a set of weights, including weights for the redshift failure, w_{zf} , close pair due to fiber collisions, w_{cp} and for systematics due to the effect of completeness, the variation of the mean density as a function of stellar density and Galactic extinction, w_{sys} . In addition, the FKP weight to minimize the variance in the clustering measurement combining regions (Feldman

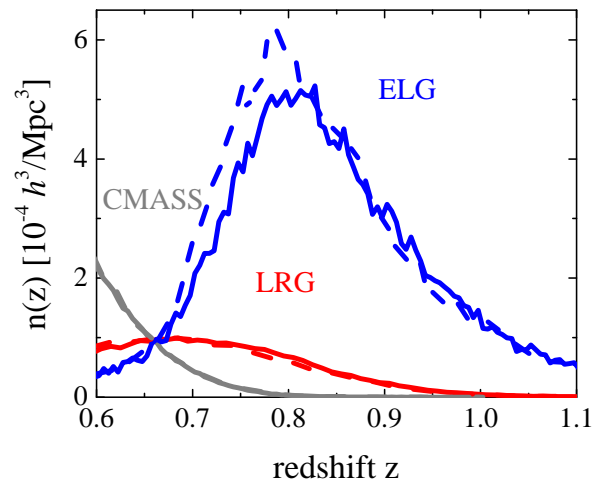


Figure 1. The volume density as a function of redshift for eBOSS DR16 LRG (red), BOSS DR12 CMASS (grey), and eBOSS DR16 ELG (blue) samples. The distribution in North Galactic Cap is shown in solid curves and South Galactic Cap in dashed curves.

et al. 1994) is added

$$w_{\text{FKP}} = \frac{1}{1 + n(z)P_0}, \quad (1)$$

where $n(z)$ is the number density of galaxies, and P_0 is set to $10,000 h^{-3} \text{ Mpc}^3$. The total weight applied to each eBOSS LRG is (Ross et al. 2020)

$$w_{\text{tot}}^{\text{LRG}} = w_{\text{FKP}} \times w_{\text{sys}} \times w_{\text{cp}} \times w_{\text{zf}}. \quad (2)$$

The eBOSS DR16 LRG sample overlaps with the BOSS DR12 CMASS in the redshift range of $0.6 < z < 1.0$ (Reid et al. 2016), as shown in Figure 2, thus these two catalogs are merged into one sample, dubbed ‘LRGpCMASS’, in this work. Note that the BOSS DR12 CMASS used different procedures for generating close-pair and redshift failure weights and the total weight is counted via (Reid et al. 2016)

$$w_{\text{tot}}^{\text{CMASS}} = w_{\text{FKP}} \times w_{\text{sys}} \times (w_{\text{cp}} + w_{\text{zf}} - 1). \quad (3)$$

The combined DR16 BOSS+eBOSS LRG catalogue includes the correct total weight for each LRG in order to avoid confusion (see Section 5.7 of Ross et al. 2020 for more details).

2.2 The eBOSS ELG sample

The target sample of emission line galaxies is selected from the DECam Legacy Survey (DECaLS) grz -photometry (Raichoor et al. 2017), which provides an imaging dataset at higher redshifts. The final large-scale structure catalogue creation is described in the companion paper (Raichoor et al. 2020). We use the complete eBOSS DR16 ELG catalogues in the redshift range of $0.6 < z < 1.1$, which is composed of 83,769 galaxies in the NGC and 89,967 galaxies in the SGC with spectroscopic redshifts. The redshift distributions in NGC and SGC are shown in blue solid and dashed curves in Figure 1. The eBOSS DR16 ELG sample overlaps with LRGpCMASS within $0.6 < z < 1.0$. The effective sky area of ELG is 369.4 deg^2 in NGC and 357.5 deg^2 in SGC, which are shown in blue regions of Figure 2. The overlapping area covered ELG and LRGpCMASS samples is $\sim 730 \text{ deg}^2$.

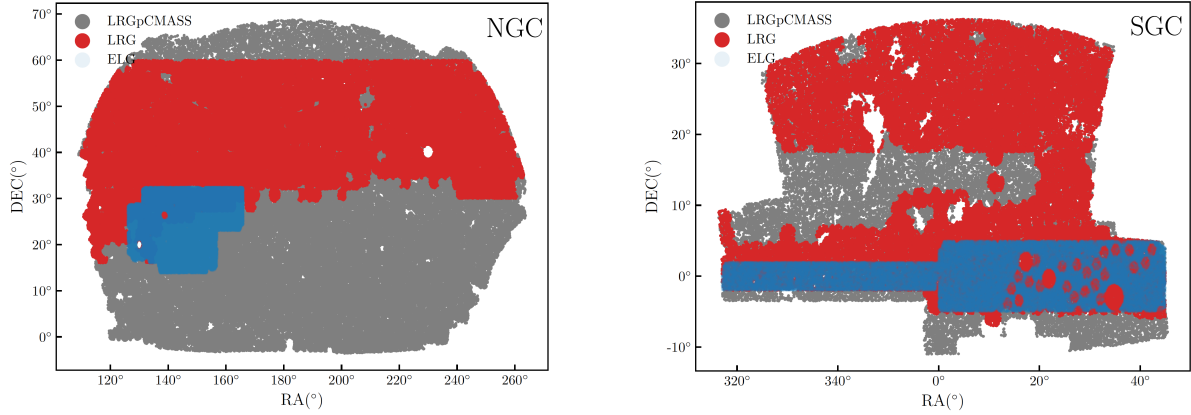


Figure 2. Footprint of eBOSS DR16 LRG (red) and ELG (blue), and a combined sample of eBOSS DR16 LRG and BOSS DR12 CMASS (grey) in the North Galactic Cap (NGC, left) and South Galactic Cap (SGC, right).

The total weight assigned to each eBOSS ELG is

$$w_{\text{tot}}^{\text{ELG}} = w_{\text{FKP}} \times w_{\text{sys}} \times w_{\text{cp}} \times w_{\text{zf}}; \quad (4)$$

here $P_0 = 4000 h^{-3} \text{Mpc}^3$ in w_{FKP} . A description of the observational effects is presented in Raichoor et al. (2020).

The ELG sample suffers from angular systematics, which could be due to the photometry of the imaging observation used for target selection, and this kind of observation systematics may bias the measurement of galaxy clustering (de Mattia et al. 2020; Tamone et al. 2020). Burden et al. (2017) proposed a modified model of correlation function to null the angular modes from the galaxy clustering, such that the contamination from angular systematics can be largely reduced. A sophisticated model is developed by Paviot et al. (2020), which is used for this analysis.

2.3 The radial integral constraint

The true radial selection function in spectroscopic surveys is difficult to determine from the survey itself, and it is commonly approximated from the redshift distribution of the actual data sample. When generating the corresponding random catalogue, the redshifts of data are assigned to the random catalogues, dubbed the *shuffled* scheme. This ensures that the average density fluctuations along the LOS are zero, but leads to an impact on the galaxy clustering on large scales. This effect is called as the radial integral constraint (RIC). The scheme to correct the RIC effect in theory was proposed by de Mattia & Ruhlmann-Kleider (2019). This modelling method is used to account for the correction of RIC effect in the analysis of eBOSS DR16 ELG clustering (see e.g. de Mattia et al. (2020); Tamone et al. (2020)). Alternatively, we can subtract the RIC effect from the data measurement. Firstly we quantify the RIC effect using additional two sets of EZmocks without systematics (Zhao et al. 2020a). One set of mocks contains the RIC effect, in which the redshifts of the random catalogues are assigned from the redshifts of each mock data via the *shuffled* scheme. The other set is without the RIC effect, where 1000 mock datasets use a single random catalogue sampling the redshift distribution of data (dubbed the *sampled* scheme). The difference between these two sets of mocks provides an estimation of the RIC effect, which then can be subtracted from the data measurement. We are aware that

this is an approximation, as the dependence of the RIC on cosmological parameters is not accounted for in this scheme. We performed a comparison with the forwarding modelling method and find the difference is negligible given the statistical uncertainty of the ELG sample.

2.4 The effective redshift

The effective redshift of the sample is determined via the following weighted pair-count,

$$z_{\text{eff}} = \frac{\sum w_i^m w_j^n (z_i^m + z_j^n)/2}{\sum w_i^m w_j^n}, \quad (5)$$

where w_i is the total weight of the i th galaxy at redshift z_i . We compute the effective redshift over all galaxy pairs separated by a distance between 25 and $150 h^{-1} \text{Mpc}$,¹ having $z_{\text{eff}} = 0.70$ for the combined sample of NGC and SGC LRGpCMASS when $m = n = \text{L}$, $z_{\text{eff}} = 0.845$ for the ELG combined sample in NGC and SGC when $m = n = \text{E}$, and $z_{\text{eff}} = 0.77$ for the cross galaxy pairs between LRGpCMASS and ELG samples, i.e. $m = \text{L}$ and $n = \text{E}$.

3 MOCK CATALOGUES

In this section we present the mock datasets, on which we will perform series of tests to check our pipeline of analysis, including the modeling and parameter estimation.

3.1 MDPL2 mocks

To test our modelling of non-linear gravitational collapse and certain aspects of galaxy physics, we generate mock catalogues using the Multi-tracer Halo Occupation Distribution (MTHOD; Alam et al. 2019). The MTHOD approach introduces a new way to model multiple tracers in the same volume. In this approach each of the tracers can have its own occupation recipe for the central

¹ The limits of separations have little effect on the value of the effective redshift.

and satellite galaxies. MTHOD ensures that the joint probabilities of occupation are well behaved by limiting the total probability of central galaxies in a halo to 1 and makes sure that non-physical behaviour is forbidden, such as multiple types of galaxies at the centre of the same dark matter halo. The key parameters in MTHOD models involve the independent parameters for the occupation probability of central and satellite galaxies for each tracer. The MTHOD mock galaxy catalogue is created using the MultiDark Planck simulation (MPDL2; Prada et al. 2012) publicly available² through the CosmoSim database. MPDL2 is a dark matter only N -body simulation using the Gadget-2 algorithm (Klypin et al. 2016). MDPL2 assumes a flat Λ CDM cosmology with $\Omega_m = 0.307$, $\Omega_b = 0.048$, $h = 0.67$, $n_s = 0.96$ and $\sigma_8 = 0.82$, and is a periodic box of side length $1h^{-1}\text{Gpc}$ sampled by 3840^3 particles. A halo catalogue is generated using the ROCKSTAR halo finder (Behroozi et al. 2013) at an effective redshift of $z = 0.86$.

The DM haloes are then populated using the following equations for central and satellite galaxies as a function of halo mass, M_{halo} :

$$p_{\text{cen}}^{\text{tot}}(M_{\text{halo}}; \vec{\theta}) = \sum_{\text{tr} \in \text{TR}} p_{\text{cen}}^{\text{tr}}(M_{\text{halo}}; \theta^{\text{tr}}) \quad (6)$$

$$\langle N_{\text{sat}}^{\text{tot}} \rangle(M_{\text{halo}}; \vec{\theta}) = \sum_{\text{tr} \in \text{TR}} \langle N_{\text{sat}}^{\text{tr}} \rangle(M_{\text{halo}}; \theta^{\text{tr}}), \quad (7)$$

where the sum is over all tracers in the list, $\text{TR} = \{\text{LRG}, \text{QSO}, \text{ELG}\}$. This equation requires a constraint of $p_{\text{cen}}^{\text{tot}} \leq 1$ for any halo mass. The explicit forms of $p_{\text{cen}}^{\text{tr}}$ and $\langle N_{\text{sat}}^{\text{tr}} \rangle$ are given in equations 8-14 in Alam et al. (2019). The full list of parameters ($\theta = \{\theta^{\text{LRG}}, \theta^{\text{ELG}}, \theta^{\text{QSO}}\}$) and best-fit values obtained for the eBOSS samples are given table 1 of Alam et al. (2019). All three tracers (i.e. LRG, ELG and QSOs) are modelled within the MTHOD framework. However, we only use the LRG and ELG galaxies, and do not use the QSOs from the default in this paper. The number of LRG galaxies is 156,800 and the number of ELG galaxies is 3,301,753, with a much higher volume density of ELGs than that of LRGs. Two different models are used to populate the central galaxy called standard HOD (SHOD) and High Mass Quenched (HMQ) model. We create six realisations for each mock catalogue by projecting RSD along different axes of the cubic box.

3.1.1 The semi-analytic covariance matrix

In this analysis, we have six non-trivial combinations of correlation function multipoles, each of which has 25 bins. This leads to a total of 11325 independent covariance matrix elements, thus the covariance requires significant computational power to compute. As an alternative, we consider semi-analytic methods, in particular the RascalC method (Philcox & Eisenstein 2019; Philcox et al. 2020), which is a fast algorithm for computing two- and three-point correlation function covariances in arbitrary survey geometries. This works by noting that, in the Gaussian limit, the covariance can be written as an integral of products of the correlation function over four copies of the survey window function, which can be rapidly evaluated using importance sampling and random particle catalogues. Non-Gaussianity can be added via a small rescaling of the shot-noise terms, shown to be an excellent approximation on BAO scales in O’Connell et al. (2016) and O’Connell & Eisenstein (2019)). Using RascalC it is possible to estimate covariance

matrices from an observational dataset and window function alone, drastically reducing the dependence on mocks and hence the computational resources required.

Here, we estimate the covariances for the periodic MDPL2 mocks, using all non-trivial combinations of LRG, ELG and cross correlation functions. As an input we require estimates of the correlation function computed over a large range of radii; these are estimated from the mocks using bins of width $\Delta r = 2h^{-1}\text{Mpc}$ from $r = 0h^{-1}\text{Mpc}$ to $r = 200h^{-1}\text{Mpc}$ and ten angular bins. For efficient configuration-space sampling we use random particle catalogues, which, given the periodic geometry, are here simply sets of $\sim 10^6$ particles uniformly placed on the cube for both LRGpC-MASS and ELG samples. In total, we sample $\sim 10^{14}$ quadruplets of points in configuration-space to build a smooth model, which requires ~ 400 CPU-hours in total, significantly less than that required for traditional mock-based analyses.

3.2 The EZmocks

To estimate the covariance matrices of the clustering measurements of the full eBOSS data, we rely on 1000 realisations of multi-tracer EZmock catalogues, for both LRGs and ELGs. These mocks are based on dark matter density fields generated using the Zel’dovich approximation (Zel’dovich 1970). Galaxies are then sampled in the density field with effective bias descriptions. The bias models for LRGs and ELGs are calibrated separately to the eBOSS data, with four free parameters. Nevertheless, the underlying dark matter density fields for different tracers are evolved from the same initial conditions, to account for their cross correlations. As the result, the cross correlation function between the EZmock LRGs and ELGs are well consistent with that of the data on small scales (for details, see Zhao et al. 2020a).

In this work we use three different sets of EZmocks. Two of them are free of observational systematics, with only survey footprint, veto masks, and radial selections applied, which are used to estimate the RIC effect mentioned in Sec. 2.3. The random catalogues for these two sets of mocks are generated using the *sampled* and *shuffled* schemes respectively. For the *sampled* random catalogues, the redshift distributions are sampled from the spline-smoothed $n(z)$ of the data, while for the *shuffled* randoms, the redshifts are taken directly from the corresponding galaxy catalogues. The third set of EZmocks contain various observational effects, such as photometric systematics, fiber collisions, and redshift failures. These contaminated mocks are used to measure the covariance matrices of our analysis.

4 THE TEMPLATE FOR THE FULL SHAPE ANALYSIS

We use the ‘Gaussian streaming model’ (GSM) developed in Reid & White (2011) to compute the theoretical correlation function:

$$1 + \xi(s_{\perp}, s_{\parallel}) = \int \frac{dy}{\sqrt{2\pi [\sigma_{12}^2(r, \mu) + \sigma_{\text{FoG}}^2]}} [1 + \xi(r)] \times \exp \left\{ -\frac{[s_{\parallel} - y - \mu v_{12}(r)]^2}{2 [\sigma_{12}^2(r, \mu) + \sigma_{\text{FoG}}^2]} \right\}, \quad (8)$$

where $s_{\parallel} \equiv s\mu$ and $s_{\perp} \equiv s\sqrt{(1 - \mu^2)}$ denotes the separation of pairs along and across the LOS, respectively; $\xi(r)$ is the real-space correlation function as a function of the real-space separation r ; $v_{12}(r)$ is the mean infall velocity of galaxies separated by r ; and $\sigma_{12}(r, \mu)$ is the pairwise velocity dispersion of galaxies. The

² <https://www.cosmosim.org/cms/simulations/mdpl2/>

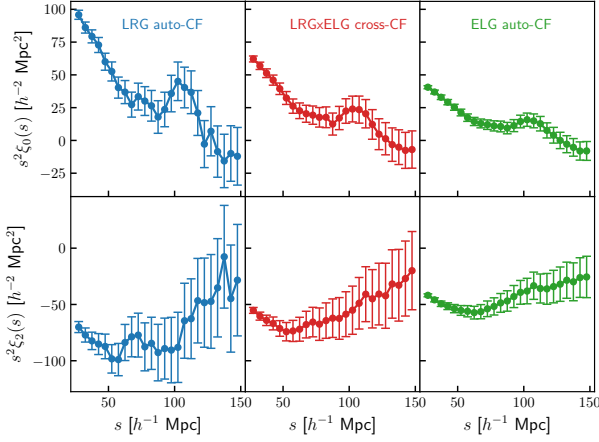


Figure 3. The measured monopole (upper panels) and quadrupole (bottom panels) of the correlation function from a set of MDPL2 mocks following the multi-tracer HMQ HOD model. The LOS is set to be along the z axis. The 1σ error bar is estimated from the RascalC covariance matrix.

parameter σ_{FOG} is used to marginalize over the Fingers-of-God (FoG) effect on nonlinear scales due to random motions of galaxies. The quantities $\xi(r)$, $v_{12}(r)$ and $\sigma_{12}(r, \mu)$ are computed using the Convolution Lagrangian Perturbation Theory (CLPT),³ (Carlson et al. 2013; Wang et al. 2014)

$$1 + \xi(r) = \int d^3q M_0(r, q) \quad (9)$$

$$v_{12,i}(r) = [1 + \xi(r)]^{-1} \int d^3q M_{1,i}(r, q) \quad (10)$$

$$\sigma_{12,ij}^2(r) = [1 + \xi(r)]^{-1} \int d^3q M_{2,ij}(r, q), \quad (11)$$

where $v_{12,i}(r)$ is the component of mean pairwise velocity along the direction of pairwise separation \hat{r}_i , and $\sigma_{12,ij}^2(r)$ is the velocity dispersion component along the pairwise separation vector \hat{r} . $M_0(r, q)$, $M_{1,i}(r, q)$ and $M_{2,ij}(r, q)$ are the convolution kernels that depend on the linear matter power spectrum and the first two non-local derivatives of the Lagrangian bias, *i.e.* $\langle F' \rangle$ and $\langle F'' \rangle$ (see Wang et al. 2014 for more details).

As mentioned in Sec. 2.2, for the auto-correlation function of ELG, we need to account for a correction to the angular systematics in the modelling. Such a template of the modified correlation function, as shown below, developed by Paviot et al. (2020) can well mitigate the angular contamination.

$$\begin{aligned} \tilde{\xi}(s_{\perp}, s_{\parallel}) &= \xi(s_{\perp}, s_{\parallel}) \\ &- \frac{2 \int \xi(s_{\perp}, s'_{\parallel}) n[\chi(z_{\text{RP}}) - s'_{\parallel}/2] ds'_{\parallel}}{\int n(\chi) d\chi} \\ &+ \frac{\int n^2(\chi) d\chi \int \xi(s_{\perp}, s'_{\parallel}) ds'_{\parallel}}{[\int n(\chi) d\chi]^2}, \end{aligned} \quad (12)$$

where $n(\chi)$ is the radial selection function of the survey, χ is the comoving distance out to a galaxy at redshift z , and the parameter $z_{\text{RP}} = 0.84$ is determined by minimizing the difference between the mean of the modified correlation function multipoles from two

sets of ELG EZmocks (with and without systematics), as performed in Tamone et al. (2020).

The CLPT-GSM model can be easily generalised to model the cross-correlations between two tracers with different biases via the following transformation (Carlson et al. 2013; Wang et al. 2014),

$$\langle F' \rangle \rightarrow \frac{1}{2} (\langle F'_m \rangle + \langle F'_n \rangle) \quad (13)$$

$$\langle F'' \rangle \rightarrow \frac{1}{2} (\langle F''_m \rangle + \langle F''_n \rangle) \quad (14)$$

$$\langle F' \rangle^2 \rightarrow \langle F'_m \rangle \langle F'_n \rangle \quad (15)$$

$$\langle F'' \rangle^2 \rightarrow \langle F''_m \rangle \langle F''_n \rangle \quad (16)$$

$$\langle F' \rangle \langle F'' \rangle \rightarrow \frac{1}{2} (\langle F'_m \rangle \langle F''_n \rangle + \langle F''_m \rangle \langle F'_n \rangle). \quad (17)$$

Here the first local Lagrangian bias $\langle F' \rangle$ is related to the Eulerian linear bias factor b via,

$$b = 1 + \langle F' \rangle, \quad (18)$$

and the second local Lagrangian bias $\langle F'' \rangle$ is fixed under the peak-background split assumption using the Sheth-Tormen mass function (Sheth & Tormen 1999).

The separation *i.e.* $(s'_{\perp}, s'_{\parallel})$ in the true cosmology might be different from those $(s_{\perp}, s_{\parallel})$ in the fiducial cosmology, which is used to convert the redshifts to distances. This is known as the AP effect (Alcock & Paczynski 1979), which can be accounted for via the following relation:

$$s'_{\perp} = \alpha_{\perp} s_{\perp}, \quad s'_{\parallel} = \alpha_{\parallel} s_{\parallel}. \quad (19)$$

Here, two scaling factors $(\alpha_{\perp}, \alpha_{\parallel})$ are introduced to parameterise the differences of distances (across and along the LOS) between the true and fiducial cosmology:

$$\alpha_{\perp} = \frac{D_M(z) r_d^{\text{fid}}}{D_M^{\text{fid}}(z) r_d}, \quad \alpha_{\parallel} = \frac{D_H(z) r_d^{\text{fid}}}{D_H^{\text{fid}}(z) r_d}, \quad (20)$$

where $D_M(z) \equiv (1+z)D_A(z)$, and $D_A(z)$ is the angular diameter distance. $D_H(z) = c/H(z)$, $H(z)$ is the Hubble expansion parameter. The superscript ‘fid’ denotes the corresponding values in the fiducial cosmology.

5 MEASUREMENTS OF CORRELATION FUNCTIONS

We measure the auto-correlation functions for the ELG and LRGpCMAS samples using the Landy & Szalay (1993) estimator,

$$\xi(s, \mu) = \frac{DD(s, \mu) - 2DR(s, \mu) + RR(s, \mu)}{RR(s, \mu)}, \quad (21)$$

where DD , DR and RR are the weighted data-data, data-random and random-random pair counts with the separation s , and the cosine of the angle between the pair and the LOS, denoted as μ .

Additionally, we measure the cross-correlation between these two samples using the following estimator,

$$\xi(s, \mu) = \frac{D^E D^L - D^E R^L - D^L R^E + R^E R^L}{R^E R^L}, \quad (22)$$

where superscripts ‘E’ and ‘L’ represent the ELG and LRGpCMAS samples, respectively.

The Legendre projections of the correlation function is calculated to obtain the correlation function multipoles,

$$\xi_{\ell}(s) = \frac{2\ell+1}{2} \int_{-1}^1 d\mu \xi(s, \mu) \mathcal{L}_{\ell}(\mu), \quad (23)$$

³ https://github.com/wl1745881210/CLPT_GSRSD

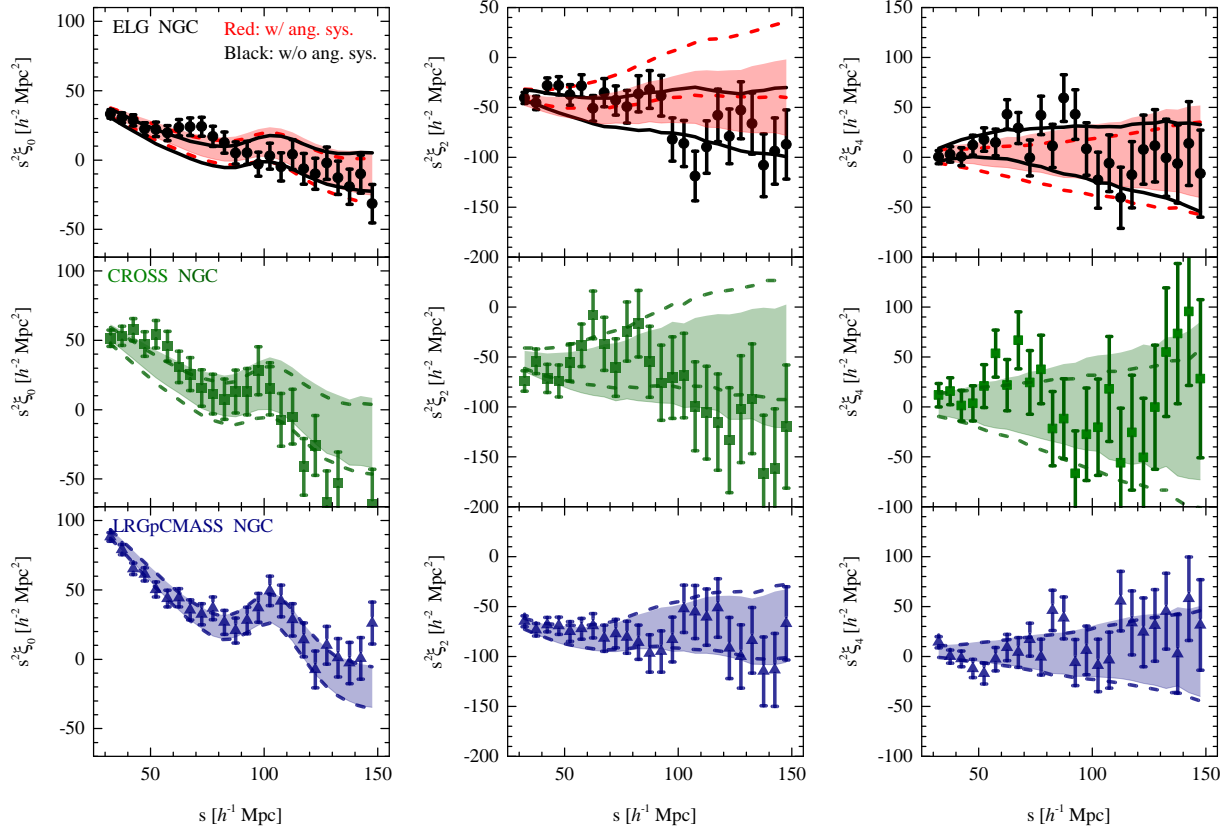


Figure 4. The measured monopole, quadrupole, and hexadecapole of correlation functions for the ELG (top, red) and LRGpCMASS (bottom, blue) samples, and their cross-correlation (middle, green) in the NGC. The 1σ error bar is calculated from EZmock covariance matrix. The dashed areas and shaded bands in each panel are the averages of multipoles with a standard deviation from EZmocks with RIC and without RIC, respectively. For the ELG sample (top panels), the black solid circles (the measurements of data samples with 1σ error bars) and black-lines regions (the mean of 1000 EZmock measurements with a standard deviation) are the measurements with the angular systematics corrected.

where $\mathcal{L}_\ell(\mu)$ is the Legendre polynomial.

In Figure 3, we present measurements of the correlation function monopole and quadrupole, including the auto-correlation functions of LRG in blue (left panels) and ELG in green (right panels), and their cross-correlation in red (middle panels), using a set of MDPL2 mock with the z LOS, which is produced via the multi-tracer HMQ HOD model. The correlation function multipoles are measured with a bin width of $5 h^{-1}\text{Mpc}$ within the scale range of $25 - 150 h^{-1}\text{Mpc}$. The error bar is estimated from the RascalC covariance matrix.

We show the correlation function multipoles measured from the DR16 galaxy samples and EZmocks in Figures 4 and 5 for measurements in the NGC and SGC, respectively. All the correlation function multipoles are measured with a bin width of $5 h^{-1}\text{Mpc}$ within the scale range of $30 - 150 h^{-1}\text{Mpc}$. The measurements of ELG are shown in upper panels, where the dashed-line and shaded areas display the 1σ regions evaluated from 1000 ELG EZmocks without and with removing the RIC effect, respectively; The black-line areas are the mean of ELG EZmocks with the 1σ standard deviation after further removing the angular systematics using Eq. 12; The black circles with the 1σ error bars are the multipoles mea-

sured from ELG samples with removing both the RIC effect and angular systematics in ELG data.

In the middle panels of Figures 4 and 5, we show measurements of cross-correlations between ELG and LRGpCMASS. The 1σ areas covered within the green dashed lines (RIC is not subtracted) and shaded regions (with RIC subtracted off) are evaluated from EZmocks. The green squares with the 1σ error bars are the measured multipoles from cross sample with the RIC effect removed. Within the 1σ region, the cross-correlation multipoles from EZmocks and data are mostly consistent on large scales.

The panels in the bottom of Figures 4 and 5 are the measured multipoles from LRGpCMASS sample and mocks. There is not much difference between blue dashed-line region (with RIC effect) and the blue shaded area (with removing RIC effect), which means that the RIC effect in LRGpCMASS data is negligible.

The covariance matrix can be estimated using the measurements of 1000 EZmocks,

$$C_{ij}^{\ell,\ell'} = \frac{1}{N-1} \sum_{k=1}^N \left[\xi_\ell^k(s_i) - \bar{\xi}_\ell(s_i) \right] \left[\xi_{\ell'}^k(s_j) - \bar{\xi}_{\ell'}(s_j) \right], \quad (24)$$

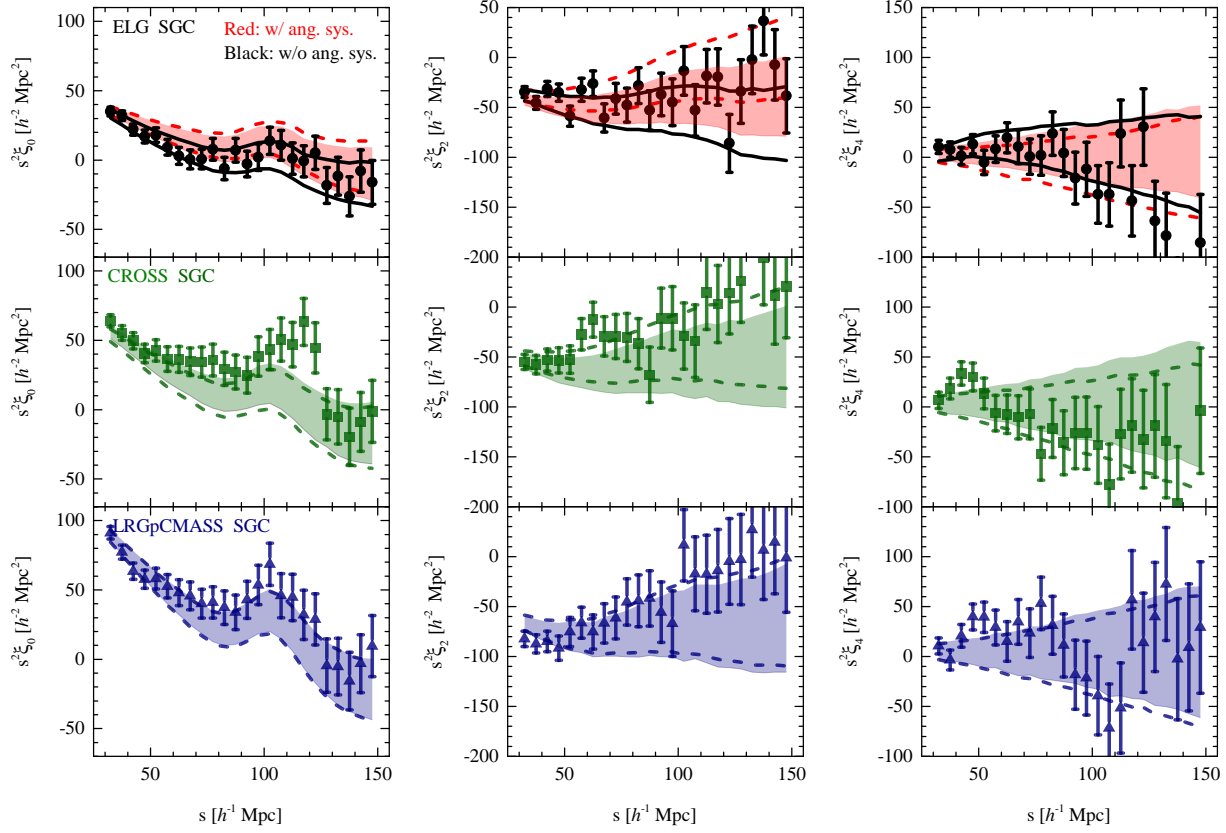


Figure 5. As Figure 4, but for the SGC.

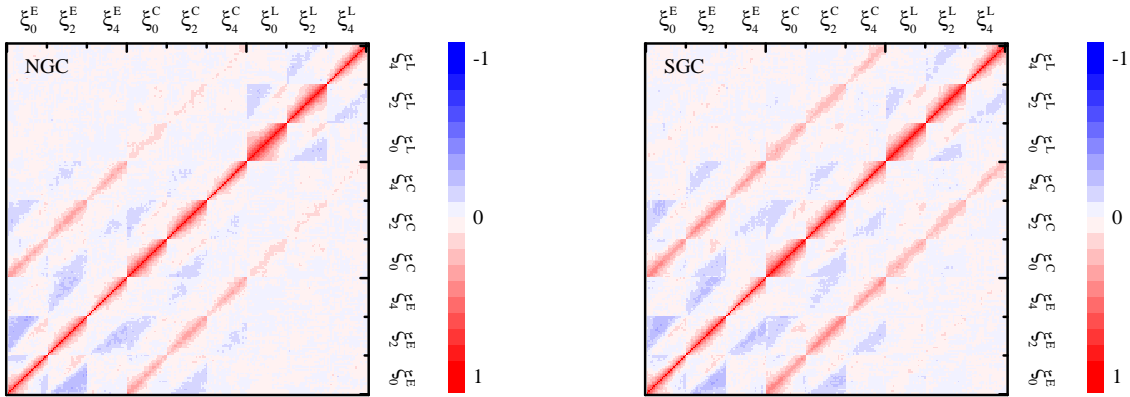


Figure 6. The correlation matrices between the correlation function monopole, quadrupole, and hexadecapole measured from 1000 EZmocks in the NGC (left) and SGC (right). For each measurement, ξ_ℓ^E , ξ_ℓ^C , or ξ_ℓ^L , we show the correlations for 24 bins linearly even spaced in separation s between 30 to $150 h^{-1} \text{Mpc}$.

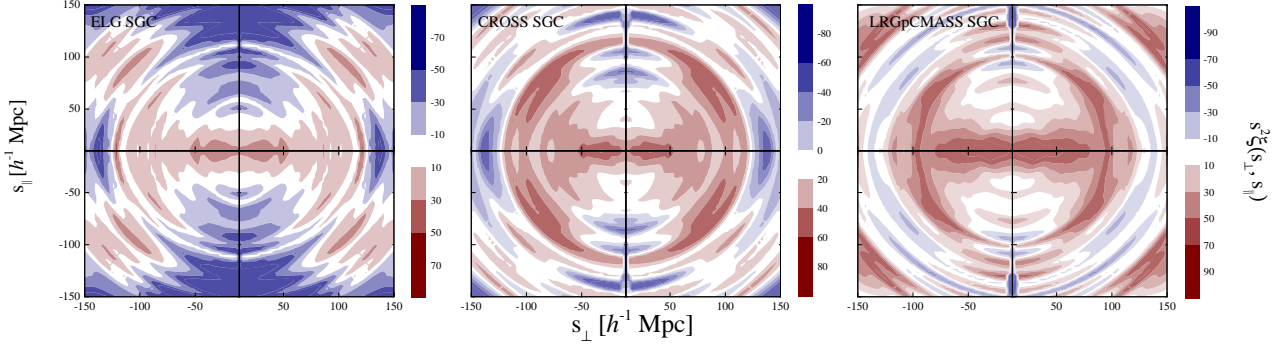


Figure 7. The 2D correlation functions assembled using the measured monopole, quadrupole and hexadecapole, *i.e.* $\xi(s, \mu) = \xi_0(s)\mathcal{L}_0(\mu) + \xi_2(s)\mathcal{L}_2(\mu) + \xi_4(s)\mathcal{L}_4(\mu)$, with $s^2 = s_{\parallel}^2 + s_{\perp}^2$, from ELG SGC samples (left), LRGpCMass SGC samples (right), and their cross-correlation (middle).

where the average multipole is given by

$$\bar{\xi}_\ell(s_i) = \frac{1}{N} \sum_{k=1}^N \xi_\ell^k(s_i), \quad (25)$$

here $N = 1000$ is the number of mock realisations. The normalised covariance matrices, *i.e.* $C_{ij}^{\ell, \ell'} / \sqrt{C_{ii}^{\ell, \ell} \times C_{jj}^{\ell', \ell'}}$, in NGC and SGC are displayed in the left and right panels of Figure 6, respectively. We fit $\xi_\ell(\ell = 0, 2, 4)$ in the range $30 < s < 150 h^{-1} \text{Mpc}$ (72 data points for each sample). The matrix contains 72×72 s bins for each tracer, and so totally there is a 216×216 covariance matrix for the combined data vector of two auto-correlation and one cross-correlation measurements.

We show the 2D correlation function reconstructed from the measured monopole, quadrupole and hexadecapole using the ELG, LRGpCMass, and their cross samples in SGC in Figure 7, where the BAO ring at $\sim 100 h^{-1} \text{Mpc}$ and the squashing effect due to RSD is clearly observed.

We quantify the Signal-to-Noise Ratio (SNR) of measurement on the cross-correlation between two tracers of eBOSS via

$$(\text{SNR})_{\xi_\ell^C}^2 = \sum_{i,j} \left[\xi_\ell^C(s_i) \right]^T F_{ij}^C \left[\xi_\ell^C(s_j) \right], \quad (26)$$

where F_{ij}^C is the inverse covariance matrix for the measured cross-correlation. We obtain a detection of the cross-correlation function at a significance of 15σ .

6 PARAMETER ESTIMATION

We perform a global fitting in the following parameter space, *i.e.*

$$\mathbf{p} \equiv \{ \alpha_{\perp}, \alpha_{\parallel}, b_{\text{NGC}}^m \sigma_8, b_{\text{SGC}}^m \sigma_8, f \sigma_8, \sigma_{\text{FoG}}^m \}, \quad (27)$$

where $m = \text{E, L, or C}$ when using the ELG, LRGpCMass, or CROSS sample alone. We use different bias parameters for NGC and SGC. Namely for the fit to each sample, we have $N_p = 6$ free parameters in each case.

For the combined fits of two samples, *e.g.* ELG + LRGpCMass, the free parameters for bias factors are

$$\begin{aligned} \{ b_{\text{NGC}}^m \sigma_8, b_{\text{SGC}}^m \sigma_8 \} &= \{ b_{\text{NGC}}^{\text{E}} \sigma_8, b_{\text{NGC}}^{\text{L}} \sigma_8, b_{\text{SGC}}^{\text{E}} \sigma_8, b_{\text{SGC}}^{\text{L}} \sigma_8 \} \\ \{ \sigma_{\text{FoG}}^m \} &= \{ \sigma_{\text{FoG}}^{\text{E}}, \sigma_{\text{FoG}}^{\text{L}} \}. \end{aligned} \quad (28)$$

In total, we have $N_p = 9$ free parameters. The number of free parameters in the cases of ELG+CROSS and CROSS+LRGpCMass are also $N_p = 9$. For the joint fit of ELG, LRGpCMass and cross samples, as the bias of the cross sample can be derived from the biases of ELG and LRGpCMass via Eq. 13, in principle we do not need to introduce additional degrees of freedom for the bias factors for the cross sample. We only assign a new damping parameter, *i.e.* $\sigma_{\text{FoG}}^{\text{C}}$ to the cross-correlation function, thus we have $N_p = 10$ free parameters for the joint fit. However, considering that the LRGpCMass and ELG samples of eBOSS DR16 are not fully overlapping, we also implement a fit by additionally introducing a set of bias parameters, *i.e.* $\{ b_{\text{NGC}}^{\text{C}} \sigma_8, b_{\text{SGC}}^{\text{C}} \sigma_8 \}$ for the cross sample. In this case the number of free parameters is $N_p = 12$.

We use a modified version of CosmoMC⁴ (Lewis & Bridle 2002) based on a Markov Chain Monte Carlo (MCMC) technique to sample the parameter space \mathbf{p} , and search for the minimum χ^2 ,

$$\chi^2(\mathbf{p}) = \chi_{\text{NGC}}^2(\mathbf{p} | b_{\text{NGC}} \sigma_8) + \chi_{\text{SGC}}^2(\mathbf{p} | b_{\text{SGC}} \sigma_8), \quad (29)$$

where

$$\begin{aligned} \chi_{\text{NGC}}^2(\mathbf{p} | b_{\text{NGC}} \sigma_8) &\equiv \sum_{i,j}^{\ell, \ell'} \left[\xi_\ell^{\text{th}}(s_i, \mathbf{p} | b_{\text{NGC}} \sigma_8) - \xi_\ell(s_i) \right] \\ &\quad F_{ij, \text{NGC}}^{\ell, \ell'} \left[\xi_{\ell'}^{\text{th}}(s_j, \mathbf{p} | b_{\text{NGC}} \sigma_8) - \xi_{\ell'}(s_j) \right], \end{aligned} \quad (30)$$

for observed multipoles $\{ \xi_\ell(s_i) \}$ and

$$\begin{aligned} \chi_{\text{SGC}}^2(\mathbf{p} | b_{\text{SGC}} \sigma_8) &\equiv \sum_{i,j}^{\ell, \ell'} \left[\xi_\ell^{\text{th}}(s_i, \mathbf{p} | b_{\text{SGC}} \sigma_8) - \xi_\ell(s_i) \right] \\ &\quad F_{ij, \text{SGC}}^{\ell, \ell'} \left[\xi_{\ell'}^{\text{th}}(s_j, \mathbf{p} | b_{\text{SGC}} \sigma_8) - \xi_{\ell'}(s_j) \right], \end{aligned} \quad (31)$$

here $F_{ij}^{\ell, \ell'}$ is the inverse of the covariance matrix in Eq. 24. An unbiased estimation for the inverse covariance matrix is given by

$$\tilde{C}_{ij}^{-1} = \frac{N - N_b - 2}{N - 1} C_{ij}^{-1}. \quad (32)$$

where N_b is the number of bins. In order to include the error propagation from the error in the covariance matrix into the fitting parameters (Percival et al. 2014) we rescale the covariance matrix,

⁴ <http://cosmologist.info/cosmomc/>

\tilde{C}_{ij} , by

$$M = \frac{1 + B(N_b - N_p)}{1 + A + B(N_p + 1)}, \quad (33)$$

here N_p is the number of the fitting parameters, and

$$A = \frac{2}{(N - N_b - 1)(N - N_b - 4)}, \quad (34)$$

$$B = \frac{N - N_b - 2}{(N - N_b - 1)(N - N_b - 4)}. \quad (35)$$

7 MOCK TESTS

We validate our pipeline in this section, using two series of mock catalogues, namely, the N-body MDPL2 mocks and 1000 realisations of the EZmocks, as introduced in Sec. 3.

7.1 MDPL2 mock fits

Figure 8 shows the $\alpha_\perp, \alpha_\parallel$ and $f\sigma_8$ parameters fitted to the MDPL2 mock. The multi-tracer MDPL2 mock has two types of HOD models, *i.e.* standard (upper panels) and HMQ (lower panels), and we consider that the LOS is along x, y or z axis, so we have six realisations in total. We perform the fit to LRG auto-correlation, ELG auto-correlation, and their cross-correlation. The corresponding constraints on the $\alpha_\perp, \alpha_\parallel$ and $f\sigma_8$ parameters from these three sets of measurement are displayed in black, red, and blue, respectively. The fitted results are generally within the error of 1% for α_\perp and α_\parallel , and the error of 3% for $f\sigma_8$. Following this, we perform a joint fit to these three sets of measurements together. The fitted results (magenta in Figure 8) are consistent with the expected values of the $\alpha_\perp, \alpha_\parallel$ and $f\sigma_8$ parameters.

7.2 EZmock tests

We apply our pipeline to the average of the correlation function multipoles, measured from 1000 realisations of the EZmocks, and present the marginalised mean values with 68% CL uncertainty of BAO and RSD parameters in Table 1 and in the left panel of Figure 9. As detailed previously, the ELG, LRGpCMass and their cross correlation can be best modelled at effective redshifts of 0.845, 0.7 and 0.77, respectively, but for the joint fit, we make an assumption that all three correlation functions can be modelled using a fixed template at $z_{\text{eff}} = 0.77$, which is explicitly tested here.

As shown in Table 1, the observables of each tracer can be well fitted by a template created at their corresponding effective redshifts, and the bias of the fitting is well within 68% CL. The fitting to the ELG sample shows a relatively larger bias, especially in $f\sigma_8$, which means that the contamination from the systematics is not completely mitigated by our pipeline. As the bias for all parameters is within the statistical uncertainty, we consider our pipeline to be accurate and proceed to apply it to the observational data, leaving further investigation of systematics to future work.⁵

We proceed to tests of all observables at $z_{\text{eff}} = 0.77$, and find almost no change on the posterior of parameters. This demonstrates that it is reasonable to model all three sets of observables at $z_{\text{eff}} = 0.77$, which is the effective redshift of the cross correlation.

The joint fitting at $z_{\text{eff}} = 0.77$ successfully returns the input values of parameters with a marginal bias, which further validates our pipeline.

7.3 Data fits

We present measurements of the BAO and RSD parameters from the DR16 samples in Table 2 and in right panel of Figure 9, and find consistent BAO and RSD measurements from ELG and LRGpCMass samples given their statistical uncertainties. Compared to results of the single-tracer analysis, the measurements of BAO and RSD from cross alone is consistent with ELG sample within the 1σ error bar. The LRGpCMass gives a much smaller statistical uncertainty than that of ELG. The difference between $f\sigma_8$ values from LRGpCMass and cross sample is 1.11σ .

Combining the ELG, LRGpCMass, and cross samples, *e.g.* ELG + CROSS, ELG + LRGpCMass, or CROSS + LRGpCMass, we obtain improved constraints. These measurements are fully consistent within 1σ error.

The joint fits from ELG and LRGpCMass auto-correlation functions and their cross correlation give the tightest constraints. For joint fits, we present the results in two cases, *i.e.* $N_p = 10$ denotes that we did not assign additional bias parameters for the cross samples, which are derived via Eq.13; $N_p = 12$ means that the cross sample has its own bias parameters. We find the BAO and RSD measurements in these two joint cases are in good agreement. Comparing with the fitted result from LRGpCMass alone, we find the Figure of Merit (FoM) of the $\alpha_\perp, \alpha_\parallel$ and $f\sigma_8$ parameters, $\text{FoM} = 1/\sqrt{\det \text{Cov}(\alpha_\perp, \alpha_\parallel, f\sigma_8)}$, from the joint ($N_p = 12$) fit is improved by a factor of 1.18. In particular, the improvement in the measurement precision of $f\sigma_8$ is 11.6% over that using only the LRGpCMass sample.

We also perform an analysis when the AP parameters are fixed to 1, as a consistency test of the fiducial cosmology. As expected, we get a tighter constraint on $f\sigma_8$ in this case, namely, the statistical uncertainty of $f\sigma_8$ with AP fixed is reduced by $\sim (25\% - 40\%)$ compared with results with AP parameters marginalized over. In cases with AP parameters fixed, we obtain a 9% improvement in the statistical precision of $f\sigma_8$ from the joint fit compared with the LRGpCMass's constraint. We compare our result on $f\sigma_8$ with AP parameters fixed with the forecast published in (Zhao et al. 2016), where the AP parameters are also fixed. Because the actual survey area is different from that used in the forecast, and the error on parameters is inversely proportional to the square root of the survey area, we preform a rescaling of the forecast using the areas, and find that the improvement on the precision of $f\sigma_8$ is 14%, which is slightly better than our actual analysis.

We derive the parameters $D_M/r_d = 18.93 \pm 0.37$ and $D_H/r_d = 19.65 \pm 0.54$ from the joint ($N_p = 12$) fitted results on α_\perp and α_\parallel in Table 2. The 1D posterior distributions of D_M/r_d , D_H/r_d , and $f\sigma_8$, and their 2D contour plots from the LRGpCMass alone (blue) and the joint fit (black) are shown in Figure 10.

For the joint fits, the best fit values and covariance matrix for the ($D_M/r_d, D_H/r_d, f\sigma_8$) parameters are given by

$$\mathbf{D} \equiv \begin{pmatrix} D_M/r_d \\ D_H/r_d \\ f\sigma_8 \end{pmatrix} = \begin{pmatrix} 18.93 \\ 19.65 \\ 0.445 \end{pmatrix}, \quad (36)$$

⁵ Note that we are using a different redshift cut for the ELG sample ($z \in [0.6, 1.1]$) from that of Tamone et al. (2020).

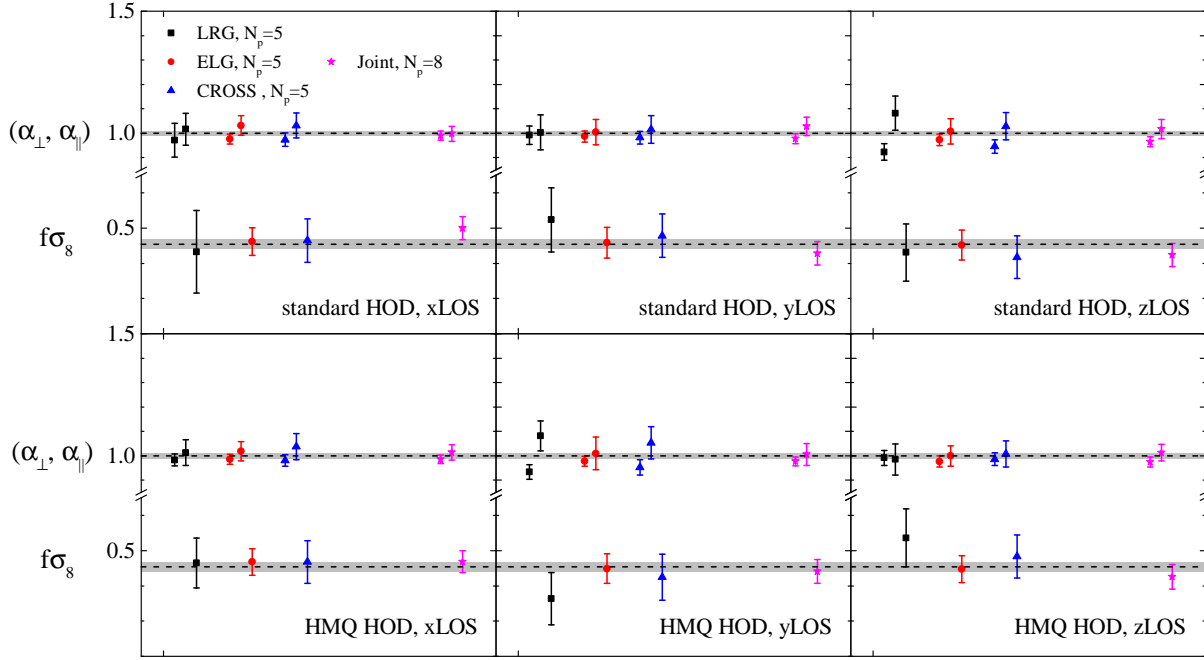


Figure 8. The best-fits from measurements of LRG and ELG mock galaxy catalogues, and their cross correlation using MDPL2 mocks in Alam et al. (2019). The shaded bands show an error of 1% on the α_{\perp} and α_{\parallel} parameters and 3% on $f\sigma_8$, and the dashed lines in the middle of the shaded area are the fiducial parameter values. The multi-tracer MDPL2 mock has two types of HOD models, *i.e.* standard (upper panels) and HMQ (lower panels) with the LOS of x, y, z , so we have six realisations in total. We fit the LRG auto-correlation (black), ELG auto-correlation (red), and their cross-correlation (blue), respectively, and then perform a joint fitting using these three sets of measurements (magenta). Note that for the MDPL2 mock sample, we do not need to assign bias parameters for NGC and SGC separately, thus the number of free parameters for the fit of each sample is $N_p = 5$, with $N_p = 8$ for the joint fit.

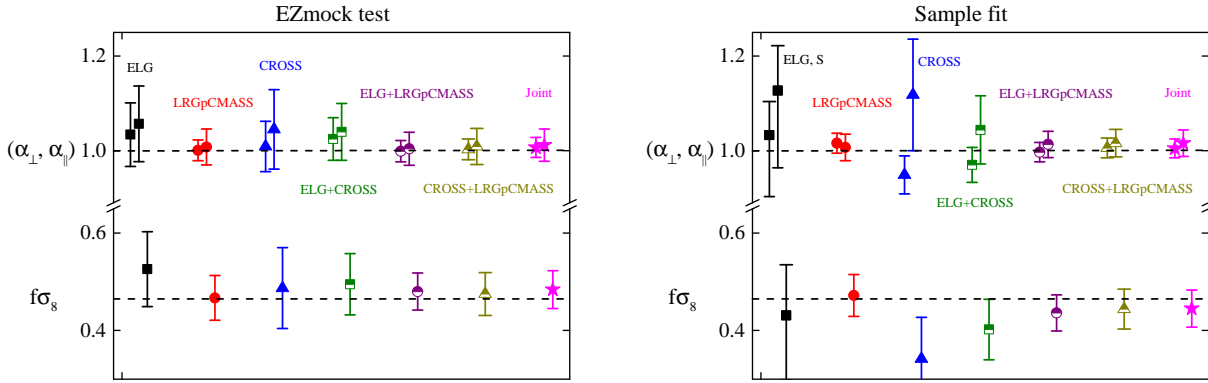


Figure 9. The mean values with 1σ error bars from EZmock tests (left) and data fits (right) of different combinations, as shown in the legend.

and

We recommend users to use the joint measurement.⁶ reported

$$C = 10^{-3} \begin{pmatrix} 137.4645 & -9.5231 & 7.3304 \\ & 293.6931 & -8.2139 \\ & & 1.4237 \end{pmatrix} \quad (37)$$

which are used in the cosmological implications section.

⁶ The multi-tracer BAO and RSD measurements and covariance matrix are available at <https://github.com/ytcosmo/MultiTracerBAORSRD/>. This measurement can be used together with the BAO and RSD measurements in the first six z bins *i.e.* $0.2 < z < 0.59$ from BOSS DR12 in (Wang et al. 2018b).

Table 1. The result of the fit to the mean of 1000 EZmocks. $\Delta(p)$ shows the difference between the mean value from mock test and its expected value. The expected values of α_\perp and α_\parallel are 1. The expected values of $f\sigma_8$ at different z_{eff} are $f\sigma_8(z_{\text{eff}} = 0.70) = 0.471$, $f\sigma_8(z_{\text{eff}} = 0.77) = 0.465$, $f\sigma_8(z_{\text{eff}} = 0.845) = 0.458$.

Catalogues	z_{eff}	$\Delta(\alpha_\perp)$	$\Delta(\alpha_\parallel)$	$\Delta(f\sigma_8)$
ELG	0.845	0.030 ± 0.066	0.048 ± 0.080	0.068 ± 0.075
ELG	0.770	0.034 ± 0.067	0.057 ± 0.080	0.061 ± 0.077
LRGpCMASS	0.700	0.001 ± 0.022	0.010 ± 0.037	-0.002 ± 0.045
LRGpCMASS	0.770	0.001 ± 0.022	0.008 ± 0.038	0.002 ± 0.046
CROSS	0.770	0.009 ± 0.053	0.045 ± 0.084	0.022 ± 0.083
ELG+CROSS	0.770	0.025 ± 0.045	0.040 ± 0.060	0.032 ± 0.063
ELG+LRGpCMASS	0.770	0.006 ± 0.022	0.011 ± 0.034	0.015 ± 0.038
CROSS+LRGpCMASS	0.770	0.003 ± 0.022	0.009 ± 0.036	0.010 ± 0.044
Joint ($N_p = 10$)	0.770	0.005 ± 0.022	0.013 ± 0.035	0.008 ± 0.039
Joint ($N_p = 12$)	0.770	0.007 ± 0.021	0.012 ± 0.034	0.013 ± 0.039

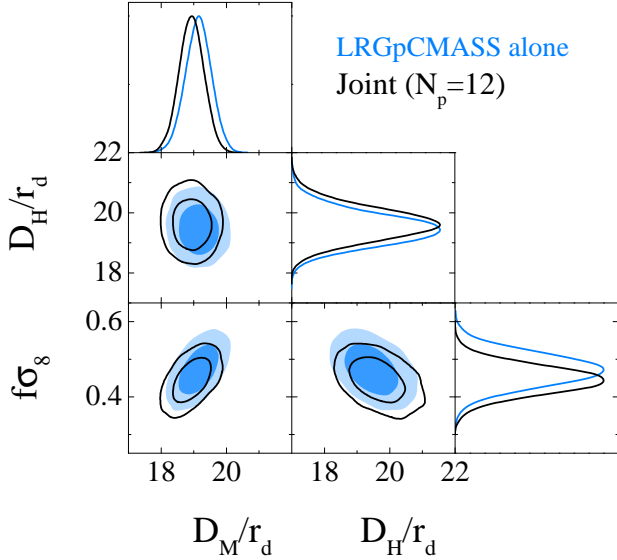


Figure 10. The one-dimensional posterior distributions and the 68 and 95 % CL contour plots for the D_M/r_d , D_H/r_d , and $f\sigma_8$ parameters using LRG samples alone (blue), and the joint constraint (black).

in Eqs. 36 and 37 to perform constraints on dark energy or tests of gravity.

In Figure 11, we present our BAO and RSD measurements alongside the Λ CDM prediction from Planck 2018 (Aghanim et al. 2018). Our measurement is consistent with these predictions.

We also show our BAO and RSD measurements and the BAO distances favored by the reconstructed dynamical dark energy from a combined observational data (Wang et al. 2018a) together in Figure 12. There is no significant tension between the new measurement and the prediction of the reconstructed dynamical dark energy within 1σ statistical error, although the measurement is more consistent with Planck 2018.

8 COSMOLOGICAL IMPLICATIONS

In this section, we briefly discuss cosmological implications of our joint measurements from the multi-tracer analysis.

We use the distance measurements to constrain the geometry of the Universe in the framework of a non-flat Λ CDM cosmology, in which the Hubble expansion rate is

$$H(z) = H_0 \sqrt{\Omega_{m0}(1+z)^3 + \Omega_{\Lambda0} + (1 - \Omega_{m0} - \Omega_{\Lambda0})}. \quad (38)$$

To avoid the dependence on r_d , we work in the parameter space of $(\Omega_{m0}, \Omega_{\Lambda0}, H_0 r_d)$.

The BAO datasets used here include the isotropic BAO measurements using MGS (Ross et al. 2015) and 6dFGRS (Beutler et al. 2011) galaxy samples; BOSS DR12 anisotropic BAO measurements in the low- and middle-redshift bins, *i.e.* ($0.2 < z < 0.5$) and ($0.4 < z < 0.6$) (Alam et al. 2016); the anisotropic BAO measurement from eBOSS DR16 quasars (Neveux et al. 2020; Hou et al. 2020), Lyman- α forest (du Mas des Bourboux et al. 2020), and our multi-tracer analysis of eBOSS DR16 ELG and LRGpCMASS.

In Figure 13, we present the 68 and 95% CL contour plots (black) for the cosmological parameters $(\Omega_{m0}, \Omega_{\Lambda0}, H_0 r_d)$, and their one-dimensional probability distributions. The joint BAO data sets a strong constraint on dark energy density, *i.e.* $\Omega_{\Lambda0} = 0.752 \pm 0.067$. The BAO alone favors the existence of dark energy at the significance of 11σ . Compared with the constraining result (*i.e.* blue contours in Figure 13) (Ata et al. 2018) using the isotropic BAO measurements using MGS (Ross et al. 2015) and 6dFGRS (Beutler et al. 2011) galaxy samples; the anisotropic BAO measurement in three z bins from BOSS DR12 (Alam et al. 2016); the isotropic BAO measurement from eBOSS DR14 quasars (Ata et al. 2018); and BOSS DR11 and DR12 Lyman- α sample (Font-Ribera et al. 2014; Bautista et al. 2017), the significance of non-zero dark energy density is improved by a factor of 1.67.

9 CONCLUSIONS

We perform a multi-tracer analysis in configuration space using the final eBOSS LRG sample combined with the BOSS CMASS sample, and the final eBOSS ELG sample.

We test the validity of the multi-tracer pipeline using the

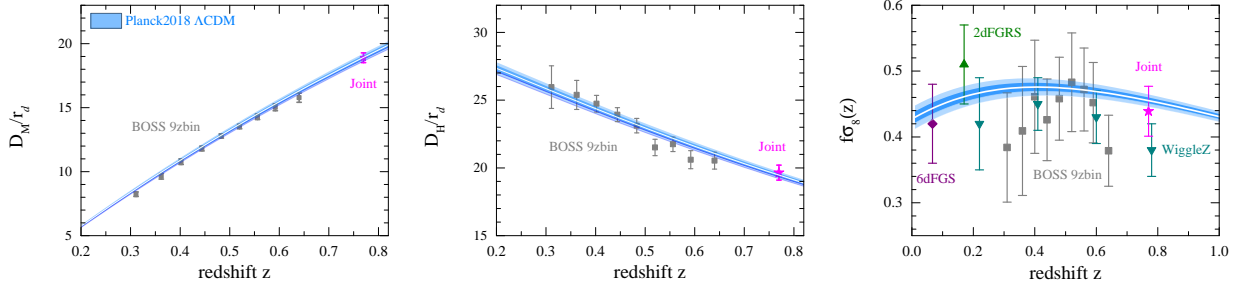


Figure 11. The evolution of D_M/r_d , D_H/r_d , and $f\sigma_8$ as a function of z . For reference, the blue bands are the predictions from Planck 2018 in the Λ CDM cosmology (Aghanim et al. 2018).

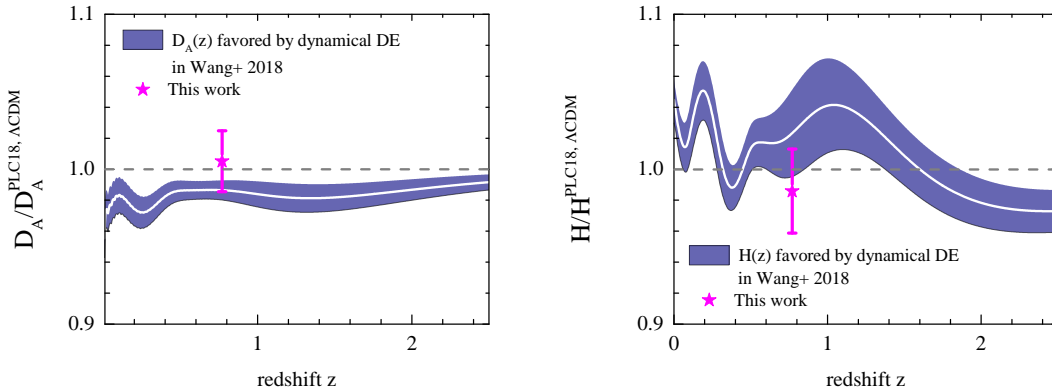


Figure 12. The shaded bands are the uncertainties of angular diameter distance, $D_A(z)$ (left) and Hubble expansion rate, $H(z)$ (right) favored by the reconstructed dynamical dark energy in (Wang et al. 2018a). The data point with error bar is our measurement in this work. They are rescaled by the mean values in the Λ CDM predicted by Planck 2018 (Aghanim et al. 2018).

N -body MDPL2 mocks and EZmocks, before applying to the analysis of real data. We report a high-precision measurement on the cosmic expansion rate and growth of structure at the effective redshift $z = 0.77$, and find an improvement in the FoM of the α_\perp , α_\parallel , $f\sigma_8$ parameters of 18% over that using the LRGpCMASS sample alone. Note that the area covered by the LRGpCMASS sample is larger by a factor of 13 than that of the ELG sample, thus the LRGpCMASS dominates the information content in the joint analysis. Even in this case, a non-trivial improvement in the FoM is contributed by the ELG sample, demonstrating the efficacy of the multi-tracer method.

We combine our measurement with previous BAO distance measurements from MGS, 6dFGS, BOSS DR12, and new BAO distance measurements from eBOSS DR16 quasars and eBOSS DR16 Lyman- α sample, to test an open Λ CDM cosmology. It is found that a non-zero dark energy density is favored by BAO alone at a 11σ significance.

The stage-IV galaxy surveys, such as the Dark Energy Spectroscopic Instrument (DESI),⁷ and Euclid,⁸ aim to observe multiple tracers with high density at higher redshifts. These surveys will explore the history of cosmic expansion and growth of structure with higher precision, taking advantage of the multi-tracer nature of the survey. Admittedly, this requires a concerted effort to min-

imize systematics, both through better theoretical modeling and a deeper understanding of observational effects.

DATA AVAILABILITY

The correlation functions, covariance matrices, and resulting likelihoods for cosmological parameters are (will be made) available (after acceptance) via the SDSS Science Archive Server (<https://sas.sdss.org/>), with the exact address to be updated later.

ACKNOWLEDGEMENTS

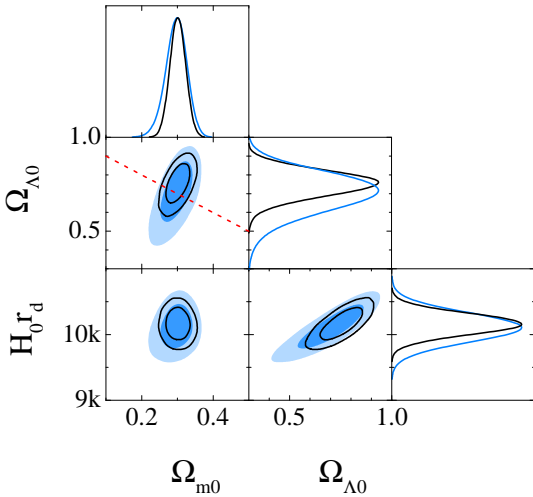
YW and GBZ are supported by NSFC Grants 11890691, 11925303, 11720101004 and 11673025. GBZ is also supported by the National Key Basic Research and Development Program of China (No. 2018YFA0404503), and a grant of CAS Interdisciplinary Innovation Team. YW is also supported by the Nebula Talents Program of NAOC. SA and JAP are supported by the European Research Council through the COSFORM Research Grant (#670193). OHEP acknowledges funding from the WFIRST program through NNG26PJ30C and NNN12AA01C. GR acknowledges support from the National Research Foundation of Korea (NRF) through Grants No. 2017R1E1A1A01077508 and No. 2020R1A2C1005655 funded by the Korean Ministry of Education, Science and Technology (MoEST), and from the faculty research fund of Sejong University.

⁷ <https://www.desi.lbl.gov/>

⁸ <https://www.euclid-ec.org/>

Table 2. The mean values with 68% CL error for the parameters, α_{\perp} , α_{\parallel} , $f\sigma_8$ from different datasets.

Samples	α_{\perp}	α_{\parallel}	$f\sigma_8$	χ^2/dof
ELG	$1.097^{+0.374}_{-0.236}$	$1.173^{+0.248}_{-0.219}$	$0.432^{+0.135}_{-0.149}$	169/138
ELG, SGC	$1.033^{+0.071}_{-0.130}$	$1.127^{+0.095}_{-0.163}$	$0.431^{+0.104}_{-0.132}$	92/67
ELG	fixed	fixed	0.433 ± 0.045	169/140
LRGpCMASS	1.016 ± 0.021	1.007 ± 0.028	0.472 ± 0.043	161/138
LRGpCMASS	fixed	fixed	0.448 ± 0.032	161/140
CROSS	0.949 ± 0.040	1.118 ± 0.118	0.342 ± 0.085	147/138
CROSS	fixed	fixed	0.443 ± 0.050	148/140
ELG+LRGpCMASS	1.004 ± 0.020	1.020 ± 0.028	0.435 ± 0.037	309/279
ELG,SGC+LRGpCMASS	1.013 ± 0.021	1.014 ± 0.028	0.451 ± 0.041	232/208
ELG+CROSS	0.970 ± 0.037	1.044 ± 0.072	0.402 ± 0.062	290/279
CROSS+LRGpCMASS	1.006 ± 0.021	1.016 ± 0.029	0.444 ± 0.041	298/279
Joint ($N_p = 10$)	1.003 ± 0.020	1.018 ± 0.030	0.439 ± 0.039	416/422
Joint ($N_p = 10$, w/ AP fixed)	fixed	fixed	0.444 ± 0.029	414/424
Joint ($N_p = 12$)	1.005 ± 0.020	1.016 ± 0.028	0.445 ± 0.038	416/420
Joint ($N_p = 12$, w/ AP fixed)	fixed	fixed	0.446 ± 0.029	414/422

**Figure 13.** The one-dimensional posterior distributions and the 68 and 95 % CL contour plots for the cosmological parameters using MGS (Ross et al. 2015) + 6dFGRS (Beutler et al. 2011) + BOSS DR12 (low- z and middle- z bins) (Alam et al. 2016) + eBOSS DR16 QSO (Neveux et al. 2020; Hou et al. 2020) + eBOSS DR16 Lyman- α forests (du Mas des Bourboux et al. 2020) + our joint ($N_p = 12$) result (black), compared with the constraining result (blue) in eBOSS DR14 paper (Ata et al. 2018). The red dashed line represents a model with zero curvature.

Funding for the Sloan Digital Sky Survey IV has been provided by the Alfred P. Sloan Foundation, the U.S. Department of Energy Office of Science, and the Participating Institutions. SDSS-IV acknowledges support and resources from the Center for High-Performance Computing at the University of Utah. The SDSS web site is <http://www.sdss.org/>.

SDSS-IV is managed by the Astrophysical Research Consortium for the Participating Institutions of the SDSS Collaboration including the Brazilian Participation Group, the Carnegie Institution for Science, Carnegie Mellon University, the Chilean Participation Group, the French Participation Group, Harvard-Smithsonian

Center for Astrophysics, Instituto de Astrofísica de Canarias, The Johns Hopkins University, Kavli Institute for the Physics and Mathematics of the Universe (IPMU) / University of Tokyo, the Korean Participation Group, Lawrence Berkeley National Laboratory, Leibniz Institut für Astrophysik Potsdam (AIP), Max-Planck-Institut für Astronomie (MPIA Heidelberg), Max-Planck-Institut für Astrophysik (MPA Garching), Max-Planck-Institut für Extraterrestrische Physik (MPE), National Astronomical Observatories of China, New Mexico State University, New York University, University of Notre Dame, Observatório Nacional / MCTI, The Ohio State University, Pennsylvania State University, Shanghai Astronomical Observatory, United Kingdom Participation Group, Universidad Nacional Autónoma de México, University of Arizona, University of Colorado Boulder, University of Oxford, University of Portsmouth, University of Utah, University of Virginia, University of Washington, University of Wisconsin, Vanderbilt University, and Yale University.

This work made use of the facilities and staff of the UK Sciama High Performance Computing cluster supported by the ICG, SEPNet and the University of Portsmouth. This research used resources of the National Energy Research Scientific Computing Center, a DOE Office of Science User Facility supported by the Office of Science of the U.S. Department of Energy under Contract No. DE-AC02-05CH11231. The authors are pleased to acknowledge that the work reported in this paper was substantially performed using the Princeton Research Computing resources at Princeton University which is consortium of groups including the Princeton Institute for Computational Science and Engineering and the Princeton University Office of Information Technology's Research Computing department.

REFERENCES

- Aghanim N. et al., 2018, arXiv:1807.06209 [astro-ph], arXiv:1807.06209
 Alam S. et al., 2015, ApJS, 219, 12
 Alam S. et al., 2016, ArXiv e-prints:1607.03155
 Alam S., Peacock J. A., Kraljic K., Ross A. J., Comparat J., 2019

- Alam S., et al., 2020, arXiv: 2007.08991
- Albareti F. D. et al., 2017, *ApJS*, 233, 25
- Alcock C., Paczynski B., 1979, *Nature*, 281, 358
- Ata M., et al., 2018, *Mon. Not. Roy. Astron. Soc.*, 473, 4773
- Bautista J. E., et al., 2017, *Astron. Astrophys.*, 603, A12
- Bautista J. E., et al., 2020, arXiv: 2007.08993
- Behroozi P. S., Wechsler R. H., Wu H.-Y., 2013, *ApJ*, 762, 109
- Beutler F. et al., 2011, *MNRAS*, 416, 3017
- Beutler F., Blake C., Koda J., Marin F., Seo H.-J., Cuesta A. J., Schneider D. P., 2016, *Mon. Not. Roy. Astron. Soc.*, 455, 3230
- Blake C., et al., 2013, *Mon. Not. Roy. Astron. Soc.*, 436, 3089
- Blanton M. R. et al., 2017, *AJ*, 154, 28
- Burden A., Padmanabhan N., Cahn R. N., White M. J., Samushia L., 2017, *J. Cosmology Astropart. Phys.*, 2017, 001
- Carlson J., Reid B., White M., 2013, *MNRAS*, 429, 1674
- Colas T., D’amico G., Senatore L., Zhang P., Beutler F., 2020, *JCAP*, 06, 001
- Cole S., Fisher K. B., Weinberg D. H., 1995, *MNRAS*, 275, 515
- Cole S. et al., 2005, *MNRAS*, 362, 505
- D’Amico G., Gleyzes J., Kokron N., Markovic D., Senatore L., Zhang P., Beutler F., Gil-Marín H., 2020, *JCAP*, 05, 005
- Dawson K. S. et al., 2016, *AJ*, 151, 44
- de Mattia A., Ruhlmann-Kleider V., 2019, *J. Cosmology Astropart. Phys.*, 2019
- de Mattia A., et al., 2020, arXiv: 2007.09008
- du Mas des Bourboux H., et al., 2020, arXiv: 2007.08995
- Eisenstein D. J. et al., 2005, *ApJ*, 633, 560
- Feldman H. A., Kaiser N., Peacock J. A., 1994, *ApJ*, 426, 23
- Font-Ribera A., et al., 2014, *JCAP*, 05, 027
- Gil-Marín H., et al., 2020, arXiv: 2007.08994
- Gunn J. E. et al., 2006, *AJ*, 131, 2332
- Hawkins E. et al., 2003, *MNRAS*, 346, 78
- Hou J., et al., 2020, arXiv: 2007.08998
- Ivanov M. M., Simonović M., Zaldarriaga M., 2020, *JCAP*, 05, 042
- Kaiser N., 1987, *Mon. Not. Roy. Astron. Soc.*, 227, 1
- Klypin A., Yepes G., Gottlöber S., Prada F., Heß S., 2016, *MNRAS*, 457, 4340
- Landy S. D., Szalay A. S., 1993, *ApJ*, 412, 64
- Lang D., Hogg D. W., Schlegel D. J., 2016, *AJ*, 151, 36
- Lewis A., Bridle S., 2002, *Phys. Rev. D*, 66, 103511
- Marín F. A., Beutler F., Blake C., Koda J., Kazin E., Schneider D. P., 2016, *Mon. Not. Roy. Astron. Soc.*, 455, 4046
- McDonald P., Seljak U., 2009, *JCAP*, 0910, 007
- Neveux R., et al., 2020, arXiv: 2007.08999
- O’Connell R., Eisenstein D., Vargas M., Ho S., Padmanabhan N., 2016, *MNRAS*, 462, 2681
- O’Connell R., Eisenstein D. J., 2019, *MNRAS*, 487, 2701
- Okumura T., Matsubara T., Eisenstein D. J., Kayo I., Hikage C., Szalay A. S., Schneider D. P., 2008, *ApJ*, 676, 889
- Pavot R., de la Torre S., et al., 2020, in prep.
- Peacock J. A. et al., 2001, *Nature*, 410, 169
- Percival W. J. et al., 2014, *MNRAS*, 439, 2531
- Percival W. J., White M., 2009, *MNRAS*, 393, 297
- Percival W. J., et al., 2001, *Mon. Not. Roy. Astron. Soc.*, 327, 1297
- Perlmutter S. et al., 1999, *ApJ*, 517, 565
- Philcox O. H., Ivanov M. M., Simonović M., Zaldarriaga M., 2020, *JCAP*, 05, 032
- Philcox O. H. E., Eisenstein D. J., 2019, *MNRAS*, 490, 5931
- Philcox O. H. E., Eisenstein D. J., O’Connell R., Wiegand A., 2020, *MNRAS*, 491, 3290
- Prada F., Klypin A. A., Cuesta A. J., Betancort-Rijo J. E., Primack J., 2012, *MNRAS*, 423, 3018
- Prakash A. et al., 2016, *ApJS*, 224, 34
- Raichoor A. et al., 2017, *MNRAS*, 471, 3955
- Raichoor A., et al., 2020, arXiv: 2007.09007
- Reid B. et al., 2016, *MNRAS*, 455, 1553
- Reid B. A., White M., 2011, *MNRAS*, 417, 1913
- Riess A. G. et al., 1998, *AJ*, 116, 1009
- Ross A. J., Samushia L., Howlett C., Percival W. J., Burden A., Manera M., 2015, *Mon. Not. Roy. Astron. Soc.*, 449, 835
- Ross A. J., et al., 2014, *Mon. Not. Roy. Astron. Soc.*, 437, 1109
- Ross A. J., et al., 2020, arXiv: 2007.09000
- Rossi G., et al., 2020, arXiv: 2007.09002
- Seljak U., 2009, *Phys. Rev. Lett.*, 102, 021302
- Sheth R. K., Tormen G., 1999, *Mon. Not. Roy. Astron. Soc.*, 308, 119
- Smee S. A. et al., 2013, *AJ*, 146, 32
- Smith A., et al., 2020, arXiv: 2007.09003
- Tamone A., et al., 2020, arXiv: 2007.09009
- Wang L., Reid B., White M., 2014, *MNRAS*, 437, 588
- Wang Y., Pogosian L., Zhao G.-B., Zucca A., 2018a, *Astrophys. J.*, 869, L8
- Wang Y., Xu L., Zhao G.-B., 2017a, *Astrophys. J.*, 849, 84
- Wang Y., Zhao G.-B., Chuang C.-H., Pellejero-Ibanez M., Zhao C., Kitaura F.-S., Rodriguez-Torres S., 2018b, *Mon. Not. Roy. Astron. Soc.*, 481, 3160
- Wang Y., et al., 2017b, *Mon. Not. Roy. Astron. Soc.*, 469, 3762
- Zel’dovich Y. B., 1970, *A&A*, 5, 84
- Zhao C., et al., 2020a, arXiv: 2007.08997
- Zhao G.-B. et al., 2016, *MNRAS*, 457, 2377
- Zhao G.-B., et al., 2017a, *Nat. Astron.*, 1, 627
- Zhao G.-B., et al., 2017b, *Mon. Not. Roy. Astron. Soc.*, 466, 762
- Zhao G.-B., et al., 2020b, arXiv: 2007.09011
- Zheng J., Zhao G.-B., Li J., Wang Y., Chuang C.-H., Kitaura F.-S., Rodriguez-Torres S., 2019, *Mon. Not. Roy. Astron. Soc.*, 484, 442